JOURNAL OF GUIDANCE, CONTROL, AND DYNAMICS
Vol. 32, No. 5, September–October 2009

Engineering Notes

Attitude Estimation from Light Curves

Charles J. Wetterer*
U.S. Air Force Academy, USAFA, Colorado 80840
and
Moriba Jah†
U.S. Air Force Research Laboratory, Kihei, Hawaii 96753

DOI: 10.2514/1.44254

I. Introduction

THE unscented Kalman filter (UKF) [1,2] has been used extensively in spacecraft attitude determination based on standard in situ measurements using gyro-based models for attitude propagation [3,4] and, more recently, in orbit determination from ground-based angles and range measurements [5]. In the latter application, the filter is unable to track changes in attitude, because these changes affect the nonconservative forces, which are subtle as compared with the dominant gravitational forces. (i.e., becoming manifest in positional data over long time scales). Attitude changes must be modeled and tracked to properly account for the nongravitational forces experienced by the object. In this Note, we describe for the first time the use of the UKF in attitude determination from ground-based brightness measurements (i.e., light curves), which are very sensitive to attitude variations. This novel application of the UKF allows for the possibility of more accurate and precise orbit determination by exploiting multi-data-type fusion, combining both astrometric and photometric observations within the same data-reduction process [5].

II. Unscented Kalman Filter

In this study, the quaternion-based attitude estimation approach of Crassidis and Markley [6] is slightly modified and used. The state vector takes a specific form:

$$\hat{x}_k^+ = \begin{bmatrix} \delta\hat{p}_k^+ \\ \boldsymbol{\omega}_k^+ \\ \hat{X}_k^+ \end{bmatrix} \tag{1}$$

where $\delta\hat{p}_k^+$ is a 3×1 vector of the error-modified Rodriguez parameters (MRPs), $\boldsymbol{\omega}_k^+$ is a 3×1 vector of the angular velocity components, and $\hat{X}_k^+$ is a $n' \times 1$ vector of any other model parameters in the state vector (such as those specifying the size, shape, and reflectance properties of the object), where $n' = n - 6$. The attitude is tracked separately by representing the inertial-to-body-frame transformation as a quaternion. The three modifications in this study from the Crassidis–Markley algorithm are as follows:

1) The initial state vector includes the angular velocity components instead of gyro biases, in which it is expected the angular velocity components are constant and so the propagated values of the angular velocity components are simply the values from the previous step.

2) Other dynamic model parameters can be included in which these are again expected to be constant and so the propagated values are the values from the previous step.

3) The full process noise covariance is added when computing the predicted state estimation error covariance (as is performed in conventional Kalman filtering) and then the sigma points are recomputed as opposed to having half the process noise added to the original sigma points (Eq. 5a in [6]), and the other half is added when computing the predicted state estimation error covariance (Eq. 8 in [6]). Regarding this final modification, in either case, the goal is to incorporate the process noise covariance into the algorithm before predicting the measurements for each sigma point.

III. Light-Curve Forward-Modeling

A light curve is the time history of an object's observed brightness. The process used to generate synthetic light curves in this study models an object as a set of facets. Each facet has a surface area, normal direction, and surface scattering law. A synthetic light curve is generated by summing over the contribution of all illuminated and observer-visible facets in the model while taking into account each facet's orientation with respect to the illumination source (the sun) and the observer. We employed a simplified version of the reflectance model of Cook and Torrance developed for computer graphics applications and the associated notation [7]. The geometry of reflection is shown in Fig. 1 (Fig. 2 from Cook and Torrance).

The reflected brightness of the object in magnitudes as measured by the observer is given by

$$m_{\text{object}} = m_{\text{sun}} - 2.5\log_{10}\left(\sum_{i=1}^{N_{\text{facets}}} \frac{S_i}{4\pi r^2}\right) \tag{2}$$

where m_{sun} is the apparent magnitude of the sun in the appropriate bandpass, r is the distance between the object and the observer, and the intensity reflected off each facet into the direction of the observer relative to the sun's apparent brightness is

$$S_i = (dR_d + sR_s)A_i\pi(\mathbf{N}_i \cdot \mathbf{L})(\mathbf{N}_i \cdot \mathbf{V}) \tag{3}$$

This depends on the diffuse bidirectional reflectance R_d, the specular bidirectional reflectance R_s, and the fraction of each to the total (d and s, respectively, where $d + s = 1$). These bidirectional reflectances are calculated using

$$R_d = w/\pi \tag{4}$$

$$R_s = \frac{DG_iF}{\pi(\mathbf{N}_i \cdot \mathbf{L})(\mathbf{N}_i \cdot \mathbf{V})} \tag{5}$$

where the facet slope distribution function D, the geometrical attenuation factor G_i, and the reflectance of a perfectly smooth surface (F) are given by

$$D = \frac{1}{m^2\cos^4\alpha}\, e^{-[\tan\alpha/m]^2} \tag{6}$$

$$G_i = \min\left\{1, \frac{2(\mathbf{N}_i \cdot \mathbf{H})(\mathbf{N}_i \cdot \mathbf{V})}{\mathbf{V} \cdot \mathbf{H}}, \frac{2(\mathbf{N}_i \cdot \mathbf{H})(\mathbf{N}_i \cdot \mathbf{L})}{\mathbf{V} \cdot \mathbf{H}}\right\} \tag{7}$$

Presented as Paper 206 at the 19th AAS/AIAA Space Flight Mechanics Meeting, Savannah, GA, 8–12 February 2009; received 20 March 2009; accepted for publication 13 April 2009.

*Professor, Department of Physics, 2354 Fairchild Drive.
†Director, Advanced Sciences and Technology Research Institute for Astrodynamics.

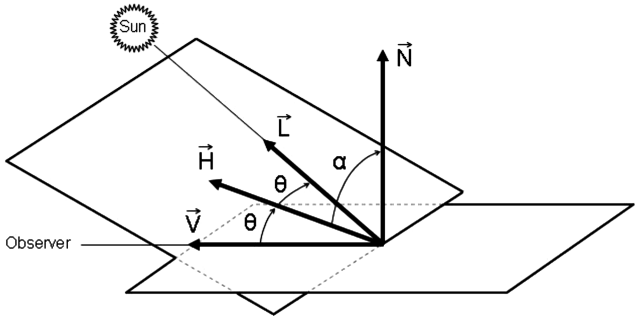

Fig. 1 The geometry of reflection.

$$F = \frac{(g-c)^2}{2(g+c)^2}\left\{1 + \frac{[c(g+c)-1]^2}{[c(g-c)+1]^2}\right\} \tag{8}$$

with $g = n^2 + c^2 - 1$, $c = \mathbf{V}\cdot\mathbf{H}$, and the index of refraction

$$n = \frac{1+\sqrt{F_0}}{1-\sqrt{F_0}}$$

where F_0 is the reflectance of the surface at normal incidence. In this study, for simplicity, the diffuse albedo and the reflectance of the surface at normal incidence are taken to be equal, $w = F_0$. In practice, the resulting magnitude from Eq. (2) is normalized to how bright the object would appear to be at a specific range (taken to be 1000 km) and corrupted by white noise.

The resulting forward model produces light curves in qualitative agreement and comparable complexity with actual observations. Figure 2 plots the light curve of an actual rotating rocket body and simulated data from the forward model (details of both are described in Sec. IV). The measurement model depends on a number of parameters, including those that describe the object's shape, surface reflectance properties, attitude, orbit, and observation circumstances. These parameters can either be assumed to be known by the model or be in the state vector and determined by the filter. In this study, the shape, orbit, and observation circumstances are always assumed to be known and the attitude is always taken to be unknown and tracked by the filter. The surface reflectance properties are either included in the state vector or not, as described in Secs. IV and V.

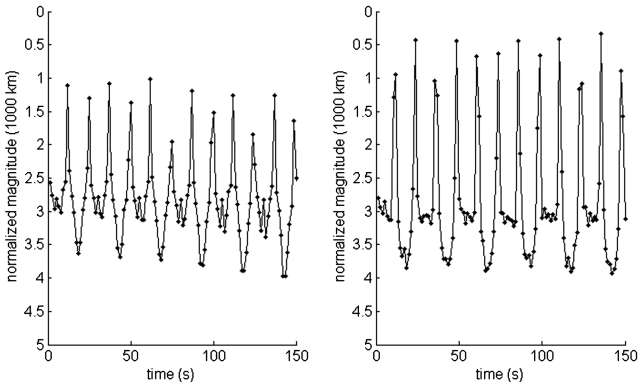

a) Actual data **b) Synthetic data**

Fig. 2 Sample light curves a) of actual data and b) from forward model.

IV. Simulated Data Test Results

The orbit and observation circumstances for the simulated data are chosen to coincide with actual data of Space Surveillance Network (SSN) 12069 (Atlas-Centaur II upper-stage rocket body in a geosynchronous transfer orbit of 244 km × 2373 km × 26°) taken by the 3.5 m Advanced Electro-Optical System (AEOS) telescope at the Maui Space Surveillance Complex (20.708°N latitude, 156.257°W longitude, and 3.075 km altitude) with a date and start time of observation of 24 March 2003 1404 hrs UTC. The model shape for the simulated rocket body is a cylinder (height = 9 m, radius = 1.5 m, $m = 0.17$, $w = 0.2$, $d = 0.3$, and $s = 0.7$) with 100 facets around its diameter and two 100-facet hemispherical end caps ($m = 0.17$, $w = 0.6$ and 0.3, $d = 0.8$, and $s = 0.2$) flattened to extend only 1 m beyond the end of the cylinder. The object's y axis is along the axis of the cylinder and the z axis is along the radius. The object is modeled as spinning solely about its z axis.

First, simulated data are generated with the axis of rotation set at a particular orientation, as represented by XYZ Euler angles ranging from $0 < \theta_x < 2\pi$, $-\pi/2 < \theta_y < \pi/2$, and $0 < \theta_z < 2\pi$ and converted to quaternion representation and the rotation rate set at $\boldsymbol{\omega} = 0\hat{x} + 0\hat{y} + 0.252\hat{z}$ rad/s with one frame every 1.316 s for 1500 steps to roughly correspond to the actual AEOS data. The measurement function is the nonlinear light-curve forward model described in Sec. III that depends not only on the quaternion-based attitude and angular velocity, but also on other parameters related to the object's shape and surface-reflection properties and other observational parameters related to the observatory site, the time of observation, and the object's orbit. The process noise covariance and measurement noise covariance can also be used to tune the UKF and are initially set at specific nonzero empirically derived values:

$$Q_k = \text{diag}[\,(2\times10^{-4})^2 \quad (2\times10^{-4})^2 \quad (2\times10^{-4})^2 \quad (10^{-12})^2 \quad (10^{-12})^2 \quad (10^{-6})^2\,]$$

and $R_k = (0.3)^2$, respectively. Finally, various initial estimates of the attitude (as expressed by the quaternion), state vector, and associated covariance are set to examine the conditions when the filter converges or not. For the quaternion, an offset to one or more of the Euler angles is applied and converted to the equivalent quaternion representation. For the initial state vector, the error MRPs and x and y components of the angular velocity are set to zero and an offset to the z component of the angular velocity is applied. The initial state covariance is chosen such that the maximum initial offsets are within 3σ from the actual values. Specifically,

$$P_0^+ = \text{diag}[\,(0.2)^2 \quad (0.2)^2 \quad (0.2)^2 \quad (10^{-12})^2 \quad (10^{-12})^2 \quad (10^{-3})^2\,]$$

.

The UKF successfully determines the correct parameters even when starting with multiple offsets. As an example, Fig. 3 displays the residuals (error from truth) of the XYZ Euler angles and the XYZ body rates for a specific case. The Euler angles at each step are derived from the quaternion with the uncertainty derived by equating the error MRP portion of the state covariance to the square of the uncertainties in the Euler angles. When offsets in the initial quaternion become too large, the UKF fails to find the correct solution, because in certain situations, near-identical light curves over the span of observations are produced from different rotation-axis positions due to the symmetry of the object (i.e., a classical observability issue in estimation). In practice, offsets of up to an average of ~0.9 rad in each of the Euler angles individually and up to ~0.003 rad/s in the rotation rate are tolerable with the UKF still converging to the correct solution. The UKF also has trouble converging when the object's axis of rotation is closely aligned to the Earth's axis of rotation.

The preceding analysis assumes that the object's shape and surface properties are known exactly. When the value of one of these model

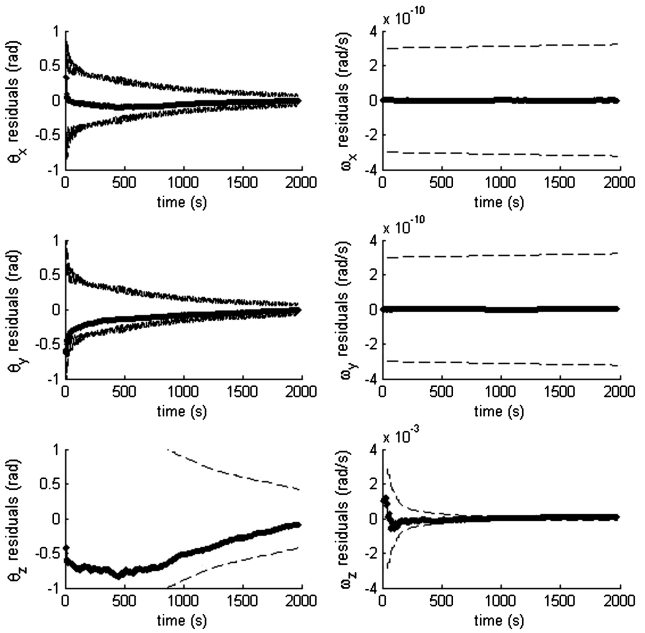

Fig. 3 Sample UKF run using rotating cylinder with $\theta_x = 0.2$ rad, $\theta_y = -0.3$ rad, $\theta_z = 1.4$, $\omega = 0.252$ rad/s, $\delta\theta_x = 0.4$ rad, $\delta\theta_y = -0.6$ rad, $\delta\theta_z = -0.4$ rad, and $\delta\omega = 0.001$ rad/s.

parameters (height, radius, albedo, slope, and ratio of diffuse to specular reflectances) is changed in the measurement model from the object's true parameters used to generate the original light curve, a systematic error between the values for which the UKF converges and the truth is introduced. For some of the parameters (e.g., albedo), the systematic error can be small despite significant deviations, whereas for other parameters (e.g., slope), the UKF may fail to converge even for slight deviations. These problems can be avoided altogether, however, by simply adding the model parameters into the state vector and allowing the filter to vary these as well while converging to the best solution. In the nomenclature of Secs. II and III, placing the surface-reflection properties of the model into the state vector results in

$$\hat{X}_0^+ = [m \quad w_{\text{cyl}} \quad d_{\text{cyl}} \quad w_{\text{end}_1} \quad d_{\text{end}_1} \quad w_{\text{end}_2} \quad d_{\text{end}_2}]^T$$

where m is the slope for all surfaces, and the albedo w and diffuse to specular fraction d for the cylinder and two ends are adjusted independently. In these simulations, it is assumed that the true state is completely unknown, and so the UKF is initiated with a variety of values covering a wide range of initial attitudes. Specifically, the first two Euler angles (which define the rotation axis) are adjusted to 24 different combinations distributed throughout the celestial sphere, and the third Euler angle (which defines an initial rotation about the body z axis) is set to the angle that would result in the first peak of the measurement function to coincide with the first specular peak of the simulated data. These are then converted to quaternions. The first six components of the initial state vector are the same as before, but now the initial state vector contains seven additional generic surface-reflection properties chosen to produce a qualitatively similar light curve of about the same brightness as the simulated data. Specifically,

$$\hat{X}_0^+ = [0.15 \quad 0.5 \quad 0.8 \quad 0.5 \quad 0.8 \quad 0.5 \quad 0.8]^T$$

The first six diagonal elements of the initial state covariance are the same as before, but now the initial state covariance contains seven additional diagonal elements related to the surface-reflection properties (all set to $(0.3)^2$).

For each case, the data are run 3 times through the UKF. The second iteration started with the end state from the first iteration and the original state covariance. The third iteration started with the end state and covariance from the second iteration. In this way, if the correct parameters are found, the residuals of the Euler angles, body rates, and other parameters during the third iteration should be nearly Gaussian about zero. The best solution is assumed to be the one in which the residuals are zero-mean white noise distributed corresponding to a solution in which the predicted axis of rotation and body rate remain most nearly fixed. The specific metric used to assess the quality of the final solutions is calculated by taking the average of the root mean square of the residuals from the final value normalized to the uncertainty from the covariance matrix for all the parameters in the state vector:

$$\text{quality} = \frac{1}{n}\left(\sum_{P=\theta_x,\theta_y\cdots d_{\text{end}_2}} \sqrt{\frac{1}{N(\sigma_P)_N}\sum_{k=1}^{N}(P_k^+ - P_N^+)^2}\right) \tag{9}$$

Smaller values of this quality metric correspond to better data fits.

Figure 4 plots the 24 initial states in the first two Euler angles connected to the corresponding final state after the third iteration (circled) for a specific case (shown in Table 1). The quality metric is listed next to each initial state. Clusters of solutions can be seen at various rotation axes, most notably at the true rotation axis and its polar opposite (both marked in Fig. 4). The true rotation axis does stand out as the one with the smallest values of the quality metric. Furthermore, the residuals in the light-curve measurements from the measurement model and in all the state parameters are well-behaved. When the attitude and surface reflectance properties for this case are then compared with the known truth, all values agree within the simultaneously derived uncertainty calculated from the state covariance (see Table 1). The UKF not only successfully found the correct attitude and surface reflectance properties simultaneously, but also provided a measure to the uncertainty in these values, given the light-curve data that produced the estimate. Other trials using simulated data with the rotation axis throughout the celestial sphere produce similar results.

V. Employing with Actual Measurement Data

Challenges remain in employing the UKF to actual brightness measurements. For example, with the comparison data used in this Note, the two ends of the actual Atlas-Centaur II upper-stage rocket body (SSN 12069) are much more complicated than flattened hemispheres, and the bidirectional reflectance distribution function (BRDF) is undoubtedly more complicated than the simple model BRDF used in the measurement function. Preliminary results using the AEOS data and an identical process as described in Sec. IV show that the filter fails to converge on single values for the various surface-reflection parameters. The rotation axis and body rates seem to converge, and in some instances, they converge to specific values for a wide range of initial conditions. With no absolute truth values to compare with and insufficient data to analyze prefit residuals, it is

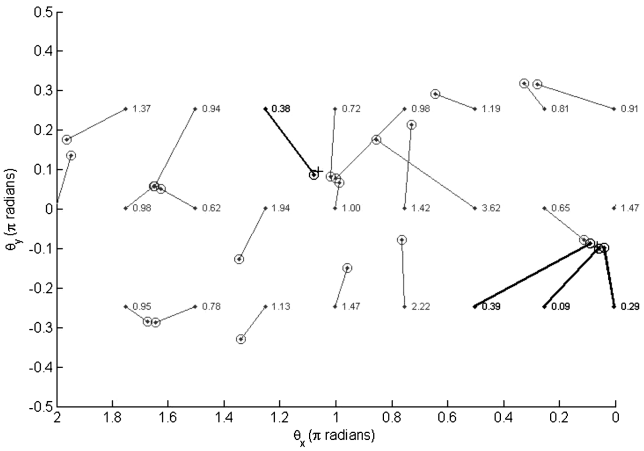

Fig. 4 Mapping of rotation-axis initial inputs to final outputs from UKF for simulated data.

Table 1 Comparison of UKF derived parameters and truth

Parameter	UKF value	UKF uncertainty	Truth
θ_x	0.19 rad	0.05	0.2
θ_y	−0.31 rad	0.03	−0.3
θ_z	1.25 rad	0.06	1.4
ω_x	0 rad/s	5×10^{-11}	0
ω_y	0 rad/s	5×10^{-11}	0
ω_z	0.25201 rad/s	0.00003	0.252
m	0.135	0.009	0.132
w_{cyl}	0.43	0.02	0.42
d_{cyl}	0.72	0.02	0.72
w_{end_1}	0.49	0.05	0.46
d_{end_1}	0.79	0.06	0.84
w_{end_2}	0.32	0.04	0.27
d_{end_2}	0.71	0.07	0.81

impossible to evaluate the filter's performance, and it is suspected that the simple measurement model used in this Note to demonstrate the concept is not sufficient. In addition, in the AEOS data for this particular rocket body, and possibly other real brightness data to be input to the filter, the bright glints off the cylindrical rocket body are saturated (see Fig. 2a) and so only represent a lower limit to the actual brightness. A way of identifying saturated data and appropriately handling it within the filter without throwing away the wealth of attitude information contained in the timing of the glint will need to be developed.

VI. Conclusions

The unscented Kalman filter is used to determine attitude information about a simulated rotating rocket body using the object's light curve. This is the first time that this has been demonstrated, and simulations show the method to be dependable when using an accurate measurement model. This application of the UKF opens up the possibility of simultaneous orbit and attitude determination by combining both astrometric and photometric observations within the same filter process, resulting in a more accurate and precise determination of both. On actual data, however, preliminary results indicate that more realistic measurement models might be required, and ongoing research regarding this as well as comparing the results with completely independent methods for determining the rotation axis and body rates for rotating rocket bodies are being explored.

Acknowledgments

The authors would like to acknowledge the U.S. Department of Defense High Performance Computing Modernization Program and Chris Sabol of the High Performance Computing Software Applications Institute for Space Situation Awareness for sponsorship of this effort. Further acknowledgement goes to U.S. Air Force Academy Cadet Cody Singletary (Class of 2009) for his summer research in testing the limits of the filter.

References

[1] Julier, S. J., and Uhlmann, J. K., "A New Extension of the Kalman Filter to Nonlinear Systems," *Proceedings of SPIE: The International Society for Optical Engineering*, Vol. 3068, Apr. 1997, pp. 182–193. doi:10.1117/12.280797

[2] van der Merwe, R., and Wan, E. A., "The Square Root Unscented Kalman Filter for State and Parameter-Estimation," *2001 IEEE International Conference on Acoustics, Speech, and Signal Processing*, Vol. 6, Inst. of Electrical and Electronics Engineers, Piscataway, NJ, May 2001, pp. 3461–3464.

[3] van der Merwe, R., and Wan, E. A., "Sigma-Point Kalman Filters for Integrated Navigation," *Proceedings of the Annual Meeting*, Inst. of Navigation, Dayton, OH, June 2004, pp. 641–654.

[4] Jah, M. K., Lisano, M. E., II, Born, G. H., and Axelrad, P., "Mars Aerobraking Spacecraft State Estimation by Processing Inertial Measurement Unit Data," *Journal of Guidance, Control, and Dynamics*, Vol. 31, No. 6, 2008, pp. 1802–1813. doi:10.2514/1.24304

[5] Jah, M., and Madler, R., "Satellite Characterization: Angles and Light Curve Data Fusion for Spacecraft State And Parameter Estimation," *Advanced Maui Optical and Optical and Space Surveillance Technologies Conference (2007 AMOS Conference)* [CD-ROM], Maui Economic Development Board, Kihei, HI, Sept. 2007.

[6] Crassidis, J. L., and Markley, F. L., "Unscented Filtering for Spacecraft Attitude Estimation," *Journal of Guidance, Control, and Dynamics*, Vol. 26, No. 4, 2003, pp. 536–542. doi:10.2514/2.5102

[7] Cook, R. L., and Torrance, K. E., "A Reflectance Model for Computer Graphics," *ACM Transactions on Graphics*, Vol. 1, No. 1, Jan. 1982, pp. 7–24. doi:10.1145/357290.357293